A Linear Projection Model to Estimate a Proton's Position in a Pencil Beam For Single Sided List Mode Proton Imaging

Helge Egil Seime Pettersen[1]†, Lennart Volz[2,3]†, Jarle Sølie[4], Dieter Röhrich[5]‡ and Joao Seco[2,3]‡.

[1]Department of Oncology and Medical Physics, Haukeland University Hospital, Bergen, Norway
[2]Division BioMedical Physics in Radiation Oncology, German Cancer Research Center (DKFZ), INF280, 69120 Heidelberg, DE
[3]Department of Physics and Astronomy, Heidelberg University, Heidelberg, Baden-Württemberg, DE
[4]Department of Electrical Engineering, Western Norway University of Applied Science, Bergen, Norway
[5]Department of Physics and Technology, University of Bergen, Norway

E-mail: `helge.pettersen@helse-bergen.no, l.volz@dkfz-heidelberg.de`

Abstract. The purpose of this work is to investigate the challenge of proton path estimation in single sided proton list-mode imaging, *i.e.*, using the available information from the pencil beam scanning system instead of a front tracking detector in combination with a rear tracking detector. A method to increase the accuracy of the path estimation in such a setup is proposed and investigated in Monte Carlo simulations.

The naïve approach is that each proton originates from the pencil beam center. In order to improve upon this, we propose a model that combines the known pencil beam phase space parameters and the measured exit vector where the proton escapes the object. The model is found to be well represented in beam spot sizes, different materials and phantom sizes by two parameters as functions of the ratio of the phantom's thickness to the proton's initial range (WET/WEPL). The optimized entrance position is then used as an input for a fast cubic spline path estimation.

The model is shown to yield a similar accuracy compared to the gold standard of the recently extended most likely path formalism for different beam energies, phantom thicknesses, materials and beam spot sizes, while being favorable in terms of implementation complexity and computational demand.

†These authors contributed equally to this work.
‡These authors share senior authorship on this work.

In conclusion, the method presented in this work serves as a simple and efficient way to estimate the proton trajectory in single sided list mode imaging setups at no loss in accuracy compared to the extended MLP formalism.

Submitted to: *Phys. Med. Biol.*
Keywords: Proton Computed Tomography, Single Sided Proton Computed Tomography, List Mode Imaging, Most Likely Path, Cubic Spline Path, Parametric Model

1. INTRODUCTION

1.1. Single Sided Proton CT

Proton imaging has gained increasingly more interest over the past decades due to the potential it offers for proton therapy — either in directly determining the relative stopping power (RSP) required for treatment planning (Zygmanski et al. 2000) or by enabling verification and optimization of the treatment plan prior to each treatment fraction (Collins-Fekete et al. 2017a).

However, the non-linear proton trajectories due to multiple Coulomb scattering (MCS) limits the achievable spatial resolution with the result that conventional X-ray CT reconstruction methods not be directly applicable to proton imaging. Therefore, in list-mode proton imaging, the trajectory of each proton through the object is commonly estimated by applying the most likely path (MLP) algorithm introduced by Schulte et al. (2008), or the phenomenological cubic spline path (CSP) approach by Collins-Fekete et al. (2015).

Optimal path estimation requires accurate information of the particles' energy, position and direction, before and after the object to be imaged. For most contemporary prototypes this is usually measured using multiple position sensitive detector planes, called the *front* and *rear* trackers (Johnson 2018). However, in single sided proton CT, as already proposed by Hanson et al. (1978), a volumetric image of the patient's RSP is calculated by measuring the protons' outgoing position and residual energy, produced by very thin pencil beams (1.6 mm FWHM) in order to achieve sufficient spatial resolution. Such a system would be especially beneficial for proton imaging at synchrotron based facilities, where the particles are delivered in bunches and not continuously: at bunch rates in the order of 100 ns, resulting in an average particle rate of at least $\sim$10 MHz. Within a bunch,

the protons are usually separated by a few nanoseconds, resulting in an effective instantaneous particle rate of >100 MHz — far above the rate capabilities of current prototypes. In order to overcome this issue, Pettersen et al. (2017) propose a pixelated range telescope able to handle such scenarios, in which a large number of protons are tracked simultaneously in a layered pixel matrix. This makes a front tracker difficult to implement — due to the high amount of scattering in the phantom, it is very difficult to correlate the hundreds of proton tracks measured before and after traversing the phantom with the envisioned prototype.

In this study, we want to explore the possibilities of estimating the individual proton's position at the patient's entrance. The naïve approach is that each proton originates from the beam spot's mean position. Any improvement over this would increase the resolution (and possibly validate the approach) of single sided list mode proton CT. An approach would be to apply the back tracker measurements as input to the Bayesian MLP framework as proposed in Krah et al. (2018). Furthermore, we will try to simplify the Bayesian method with a parametrized linear projection model (LPM) of the initial position in conjunction with a CSP to obtain the proton's estimated trajectory through the patient.

1.2. Definition of Vectors

A definition of the vectors $\mathbf{X_0}$, $\mathbf{P_0}$, $\mathbf{X_2}$ and $\mathbf{P_2}$ are given in other publications, *e.g.* in Collins-Fekete et al. (2015). In short, $\mathbf{X_0}$ is the position of a single proton at the object's entrance, and $\mathbf{P_0}$ is the directional vector $(\Delta x/\Delta z, \Delta y/\Delta z, 1)$ of the incoming proton, where $\Delta(x, y, z)$ is the difference between the two front tracker planes. $\mathbf{X_2}$ is the position of the proton exiting the object, and $\mathbf{P_2}$ is the directional vector defined similarly. The vectors $\mathbf{X_1}$ and $\mathbf{P_1}$ are here depth-dependent and give the position and direction inside the object. To aid with clarity, we denote any tracker-measured vector with a tilde $(\tilde{\mathbf{X}}_\mathbf{2}, \tilde{\mathbf{P}}_\mathbf{2})$. Also defined is the knowledge about the mean beam position and direction from the Treatment Planning System (TPS), given respectively as $\mathbf{X_0}^{\mathrm{TPS}}$ and $\mathbf{P_0}^{\mathrm{TPS}}$.

1.3. Cubic Spline Estimation of the Proton's Most Likely Path

In the framework of Collins-Fekete et al. (2015), the CSP model is calculated by introducing the two scaling factors Λ_0 and Λ_2 to account for the energy dependency of the MCS occurring inside the imaged object. Its position at any depth $t \in [0, 1]$

is calculated as

$$\mathbf{X_1}(t) = (2t^3 - 3t^2 + 1)\mathbf{X_0} + (t^3 - 2t^2 + t)\mathbf{P_{\Lambda 0}} + (-2t^3 + 3t^2)\mathbf{X_2} + (t^3 - t^2)\mathbf{P_{\Lambda 2}}, \tag{1}$$

where

$$\mathbf{P_{\Lambda 0}} = \hat{\mathbf{P}}_\mathbf{0} \cdot \Lambda_0 \cdot |\mathbf{X_2} - \mathbf{X_0}|, \qquad \mathbf{P_{\Lambda 2}} = \hat{\mathbf{P}}_\mathbf{2} \cdot \Lambda_2 \cdot |\mathbf{X_2} - \mathbf{X_0}|. \tag{2}$$

The factors Λ_0 and Λ_2 are parametrized as a function of the ratio of the object's water equivalent thickness (WET) to the initial water equivalent path length (WEPL) of the proton, repeated here for completeness:

$$\Lambda_0 = 1.01 + 0.43 \left(\frac{\text{WET}}{\text{WEPL}}\right)^2, \qquad \Lambda_2 = 0.99 - 0.46 \left(\frac{\text{WET}}{\text{WEPL}}\right)^2. \tag{3}$$

The WEPL is calculated as the PSTAR-CSDA range in water (Berger et al. 2005) at the proton's initial energy. The WET is calculated by subtracting the WEPL of the proton's residual energy from the WEPL of its initial energy, using the a cubic spline interpolation of the PSTAR-CSDA tables. This method is believed to yield higher results compared to using the Bragg-Kleeman relationship as in Collins-Fekete et al. (2015) — see Pettersen et al. (2018) for a comparison of this accuracy. Collins-Fekete et al. (2017b) show that the above CSP algorithm is equivalent to the MLP formalism as derived from the scattering theory by Williams (2004) and Schulte et al. (2008). The MLP will be described in the following section.

1.4. Bayesian Models of the Most Likely Path

The MLP of the individual protons was first implemented using a Bayesian approach, in which the Fermi-Eyges approximation to Molière's scattering theory is applied on the front and back tracker measurements and their uncertainties (Williams 2004). In order to estimate the uncertainty of different proton imaging setups, Krah et al. (2018) introduced an extended approach to the MLP. The method not only allows for an optimized path estimation in the presence of tracker uncertainties, but it can also be adapted for single sided list mode proton radiography (and CT) using the information from the TPS in place of the missing front tracker.

Since the particle scattering in the two lateral directions can be viewed as independent, the MLP estimation is usually treated as a 2D problem where the two lateral dimensions are evaluated separately. In this context, we define the

two dimensional parameter vectors that denote the particles' lateral position and direction at a given longitudinal position.

$$y_i = \begin{pmatrix} t_i \\ \theta_i \end{pmatrix}, \quad i \in \{0, 1, 2\} \tag{4}$$

Here, t denotes either one of the two lateral axes. The indices 0 and 2 mark the position at the front and rear tracker, respectively, and y_1 is the position and direction at a certain depth within the object.

To include the tracker uncertainties to the MLP estimation, Krah et al. (2018) introduce the two likelihoods $\mathcal{L}(y_0'|\tilde{y}_{0,2})$ and $\mathcal{L}(y_2'|\tilde{y}_2)$ to model the likelihood of a certain entrance and exit position $y_{0,2}'$, given the respective measurements $\tilde{y}_{0,2}$ and respective covariance matrices $\Sigma_{\text{in/out}}$. By marginalizing over all possible entrance and exit positions, they then derive a combined likelihood for the estimation of y_1 as

$$\mathcal{L}(y_1|\tilde{y}_0, \tilde{y}_2) = \iint \mathcal{L}(y_0'|\tilde{y}_0)\mathcal{L}(y_0' \to y_1)\mathcal{L}(y_1 \to y_2')\mathcal{L}(y_2'|\tilde{y}_2)\mathrm{d}y_0'\mathrm{d}y_2'. \tag{5}$$

In the case of a missing front tracker, Krah et al. (2018) use a Gaussian model to compute $\mathcal{L}(y_0'|\tilde{y}_0)$, with $\sigma_{t_{\text{in}}}$ as the beam spot size at the entrance position, and $\sigma_{\theta_{\text{in}}}$ as the angular confusion. To mirror the capabilities of Pettersen et al. (2017), we allow here for measurements of the outgoing angle $\tilde{\theta}_2$. For simplicity, we use an ideal rear tracker in this study. Using the following definitions from Krah et al. (2018) then gives the MLP in the case of a missing front tracker:

$$y_{\text{MLP}} = C_2(C_1 + C_2)^{-1}R_0 S_{\text{in}} \cdot y_0^{\text{TPS}} + C_1(C_1 + C_2)^{-1}R_1^{-1}S_{\text{out}}^{-1} \cdot \tilde{y}_2, \tag{6}$$

with

$$C_1 = R_0 S_{\text{in}} \Sigma_{\text{in}} S_{\text{in}}^{\mathsf{T}} R_0^{\mathsf{T}} + \Sigma_1 \tag{7}$$

$$C_2 = R_1^{-1}\Sigma_2(R_1^{-1})^{\mathsf{T}}. \tag{8}$$

The Gaussian pencil beam model is represented by the covariance matrix Σ_{in} and $y_0^{\text{TPS}} = \begin{pmatrix} t_0^{\text{TPS}} & \theta_0^{\text{TPS}} \end{pmatrix}^{\mathsf{T}}$, where t_0^{TPS} and θ_0^{TPS} are the mean lateral position and the mean angle of the pencil beam as obtained from the TPS, respectively, and $\tilde{y}_2 = \begin{pmatrix} \tilde{t}_2 & \tilde{\theta}_2 \end{pmatrix}^{\mathsf{T}}$ is measured using the back tracker. By using a virtual point source model with distance d_S to the isocenter, an expression for Σ_{in} can be found for a beam with lateral spread $\sigma_{t_{\text{in}}}$ and angular confusion $\sigma_{\theta_{\text{in}}}$:

$$\Sigma_{\text{in}} = \begin{pmatrix} \sigma_{t_{\text{in}}}^2 & \sigma_{t_{\text{in}}}^2/d_S \\ \sigma_{t_{\text{in}}}^2/d_S & \sigma_{t_{\text{in}}}^2/d_S^2 + \sigma_{\theta_{\text{in}}}^2 \end{pmatrix}. \tag{9}$$

S_{in} and S_{out} are the straight line projections of the measurements onto the object contour

$$S_{\text{in}} = \begin{pmatrix} 1 & d_{\text{entry}} \\ 0 & 1 \end{pmatrix}, \quad S_{\text{out}} = \begin{pmatrix} 1 & d_{\text{exit}} \\ 0 & 1 \end{pmatrix}, \tag{10}$$

where d_{entry} and d_{exit} are the physical distances of the tracker planes to the object contour. In the case of a single sided proton radiography, d_{entry} is the distance between the isocenter and the object contour. For simplicity, in this study, the isocenter was always located directly at the object entrance such that $d_{\text{entry}} = 0$ and $S_{\text{in}} = \mathbb{I}$. The scattering matrix Σ_2 and the transvection matrices R_0 and R_1 are given as

$$\Sigma_2 = \begin{pmatrix} \sigma^2_{t_2} & \sigma^2_{t_2\theta_2} \\ \sigma^2_{t_2\theta_2} & \sigma^2_{\theta_2} \end{pmatrix} \tag{11}$$

$$R_0 = \begin{pmatrix} 1 & z - z_0 \\ 0 & 1 \end{pmatrix}, \qquad R_1 = \begin{pmatrix} 1 & z_2 - z \\ 0 & 1 \end{pmatrix}. \tag{12}$$

The $\sigma^2_{t_2,\theta_2}$ are the Eyges moments, defined using the Highland equation as in Schulte et al. (2008):

$$\sigma^2_{t_2} = E_0^2 \left(1 + 0.038 \ln \frac{z_2 - z}{X_0}\right)^2 \int_z^{z_2} \frac{(z_2 - z)^2}{\beta^2 p^2} \frac{\mathrm{d}z}{X_0} \tag{13}$$

$$\sigma^2_{\theta_2} = E_0^2 \left(1 + 0.038 \ln \frac{z_2 - z}{X_0}\right)^2 \int_z^{z_2} \frac{1}{\beta^2 p^2} \frac{\mathrm{d}z}{X_0} \tag{14}$$

$$\sigma^2_{t_2\theta_2} = E_0^2 \left(1 + 0.038 \ln \frac{z_2 - z}{X_0}\right)^2 \int_z^{z_2} \frac{(z_2 - z)}{\beta^2 p^2} \frac{\mathrm{d}z}{X_0} \tag{15}$$

with $E_0 = 13.7\,\text{MeV}$, $X_0 \simeq 36.1\,\text{cm}$ being the radiation length for water and the term $1/\beta^2 p^2$ is the particles' twofold momentum-velocity function. Σ_1 is defined similarly to Σ_2, and can be obtained by exchanging z_2 with z and z with z_0 in the definition of the scattering moments.

For computations in the MLP formalism, the $1/\beta^2 p^2$ function is usually described by a 5th order polynomial function: the parameters of which are given in Schulte et al. (2008) for protons with initial energy of 200 MeV. This study, however, centers around protons with an initial energy of 230 MeV, since the system envisioned by Pettersen et al. (2017) is to be operated at that energy in the future. The parameters of the polynomial fit for this case were evaluated as given in Schulte

Parameter	Value at 200 MeV	Value at 230 MeV
a_0	7.456×10^{-6}	$5.776\,19 \times 10^{-6}$
a_1	4.548×10^{-7}	$2.197\,84 \times 10^{-7}$
a_2	-5.777×10^{-8}	$-1.239\,20 \times 10^{-8}$
a_3	1.301×10^{-8}	$3.417\,25 \times 10^{-9}$
a_4	-9.228×10^{-10}	$-2.202\,83 \times 10^{-10}$
a_5	2.687×10^{-11}	$5.682\,67 \times 10^{-12}$

Table 1. Results of the polynomial fit to the average value of the $1/\beta^2 p^2 = a_n x^n$ as a function of depth, for 200 MeV (Schulte et al. 2008) and 230 MeV protons incident on 30 cm of `G4_WATER`. The coefficients are given in units of c^2/MeV^2 divided by appropriate powers of cm.

et al. (2008): recording the kinetic energy as a function of depth for 10^5 protons incident on 30 cm of `G4_WATER` using the Geant4 MC simulation toolkit and then computing the mean $1/\beta^2 p^2$ function at steps of 5 mm. The parameters are given in table 1. For comparison purposes, 200 MeV protons were investigated as well, since this reflects the beam energy used in most contemporary studies on proton imaging.

2. LINEAR PROJECTION MODEL

2.1. Simplifying the Extended MLP Formalism

The formalism introduced by Krah et al. (2018) was developed to model the uncertainty of the MLP estimation in the context of different particle imaging setups. In this context, the marginalization of the likelihood with respect to all possible entrance and exit parameter vectors simplifies the calculation and enables a straight-forward computation of the uncertainty envelope around the MLP.

However, for the purpose of image reconstruction, the uncertainty envelope is not relevant, and the MLP estimation can be simplified. For the extended MLP, each step through the object is computed considering all possible entrance and exit positions given their respective measurements. The MLP that maximizes the likelihood in equation (5) naturally starts at the most likely entrance vector and ends with the most likely exit vector. Now, the MLP is computed based on a set of 4 measurements ($\tilde{t}_{0,2}$ and $\tilde{\theta}_{0,2}$) and therefore, the most complex trajectory that can be estimated is a cubic spline as outlined by Li et al. (2006) — this does not change even when considering measurement uncertainties. This leads to the key

observation of this study that the extended MLP introduced by Krah et al. (2018) can be obtained by estimating the most likely entrance and exit parameter vectors and then computing a CSP between them.

In general, this MLP-CSP hybrid could be computed by first deriving the optimal entrance and exit parameter vectors by maximizing the two likelihoods

$$\mathcal{L}(y_0|\tilde{y}_0, \tilde{y}_2) = \int \mathcal{L}(y_0|\tilde{y}_0)\mathcal{L}_{\Sigma_2}(y_0 \to y_2')\mathcal{L}(y_2'|\tilde{y}_2)\mathrm{d}y_2' \tag{16}$$

$$\mathcal{L}(y_2|\tilde{y}_2, \tilde{y}_0) = \int \mathcal{L}(y_2|\tilde{y}_2)\mathcal{L}_{\Sigma_1}(y_0' \to y_2)\mathcal{L}(y_0'|\tilde{y}_0)\mathrm{d}y_0' \tag{17}$$

with respect to y_0 and y_2, respectively. $\mathcal{L}(y_{0,2}|\tilde{y}_{0,2})$ depicts the likelihood from the trackers' uncertainty (or the uncertainty of the TPS pencil beam) and $\mathcal{L}(y_0 \to y_2')$ the likelihood derived from the scattering theory. All likelihoods are bi-variate Gaussians, their respective definitions were introduced by Krah et al. (2018) and are repeated here only for the sake of completeness:

$$\mathcal{L}(y_0|\tilde{y}_0) = \exp\left[-\frac{1}{2}\left(y_0 - \tilde{y}_0\right)^{\mathsf{T}} \Sigma_{\mathrm{in}}^{-1}\left(y_0 - \tilde{y}_0\right)\right] \tag{18}$$

$$\mathcal{L}_{\Sigma_{1/2}}(y_0 \to y_2) = \exp\left[-\frac{1}{2}\left(y_2 - R_{0/1}y_0\right)^{\mathsf{T}} \Sigma_{1/2}^{-1}\left(y_2 - R_{0/1}y_0\right)\right] \tag{19}$$

$$\mathcal{L}(y_2|\tilde{y}_2) = \exp\left[-\frac{1}{2}\left(y_2 - \tilde{y}_2\right)^{\mathsf{T}} \Sigma_{\mathrm{out}}^{-1}\left(y_2 - \tilde{y}_2\right)\right]. \tag{20}$$

As with the extended MLP formalism, the tracker uncertainties are included in equation (16) and equation (17) by marginalizing over all possible measurements of the parameter vector opposing the one to be optimized.

The above argumentation and the given likelihoods are applicable for any list mode proton CT setup. However, in this work we are focusing especially on single sided setups, hence, in the following, we will investigate only equation (16).

To further simplify the optimization of the entrance parameter vector, we make two assumptions: The first is (again) that of an ideal rear tracker. In the case of single sided list mode proton radiography based on the TPS information (y_0^{TPS}) and using an ideal rear tracker ($\tilde{y}_2 = y_2$), equation (16) reads:

$$\mathcal{L}(y_0|y_0^{\mathrm{TPS}}, \tilde{y}_2) = \mathcal{L}(y_0|y_0^{\mathrm{TPS}})\mathcal{L}_{\Sigma_2}(y_0 \to y_2) \tag{21}$$

The second assumption we make, is that the uncertainty of the beam delivery system regarding the beam direction is sufficiently small such that $\theta_0^{\mathrm{TPS}} \approx \theta_0$. Inserting this in equation (21) while equating the derivative of the log-likelihood

to zero yields the optimized entrance position and direction which can be used to compute an optimized lateral position t_0^{opt} to be applied as an input to the CSP formalism. We arrive at

$$t_0^{\mathrm{opt}} = \frac{\left[(\Sigma_{\mathrm{in}}^{-1})_{1,1} t_0^{\mathrm{TPS}} + (\Sigma_2^{-1})_{1,1}(\tilde{t}_2 - \theta_0^{\mathrm{TPS}} \cdot d_{\mathrm{ph}}) + (\Sigma_2^{-1})_{2,1/1,2}(\tilde{\theta}_2 - \theta_0^{\mathrm{TPS}})\right]}{\left((\Sigma_{\mathrm{in}}^{-1})_{1,1} + (\Sigma_2^{-1})_{1,1}\right)}, \quad (22)$$

where again, t marks either one of the two lateral axes. This can be re-written as

$$t_0^{\mathrm{opt}} = a\left(\tilde{t}_2 - t_0^{\mathrm{TPS}} - \theta_0^{\mathrm{TPS}} \cdot d_{\mathrm{ph}}\right) + b\left(\tilde{\theta}_2 - \theta_0^{\mathrm{TPS}}\right) + t_0^{\mathrm{TPS}}, \quad (23)$$

where

$$a = \frac{\left(\Sigma_2^{-1}\right)_{1,1}}{\left(\Sigma_{\mathrm{in}}^{-1}\right)_{1,1} + \left(\Sigma_2^{-1}\right)_{1,1}}, \qquad b = \frac{\left(\Sigma_2^{-1}\right)_{1,2/2,1}}{\left(\Sigma_{\mathrm{in}}^{-1}\right)_{1,1} + \left(\Sigma_2^{-1}\right)_{1,1}}. \quad (24)$$

The indexing $1, 2/2, 1$ remarks that the inverse scattering matrix is symmetrical, and $d_{\mathrm{ph}} = |z_2 - z_0|$ is the physical thickness of the object.

The expression for t_0^{opt} represents a weighted mean of the TPS position and the rear tracker position measurement, projected onto the front of the phantom along the beam's initial direction. The weights are computed from the pencil beam uncertainty, and the uncertainty resulting from the scattering, respectively. The term $(\Sigma_2^{-1})_{2,1/1,2}(\tilde{\theta}_2 - \theta_0^{\mathrm{TPS}})$ is a correction factor that accounts for the change in the particle direction.

Writing out the covariance for the beam spot, we find that

$$\left(\Sigma_{\mathrm{in}}^{-1}\right)_{1,1} = (d_S \sigma_{\theta_{\mathrm{in}}})^{-2} + \sigma_{t_{\mathrm{in}}}^{-2}. \quad (25)$$

Note that for an ideal parallel pencil beam, *i.e.* $\sigma_{\theta_{\mathrm{in}}} = 0$, the bi-variate Gaussian likelihood $\mathcal{L}(y_0|y_0^{\mathrm{TPS}})$ is exchanged by a simple one-dimensional Gaussian $\mathcal{L}(t_0|t_0^{\mathrm{TPS}})$ and thus $(\Sigma_{\mathrm{in}}^{-1})_{1,1}$ is exchanged by $\sigma_{t_{\mathrm{in}}}^{-2}$ in equation (23).

Alternatively, to get the optimal input vectors for the CSP algorithm, the MLP outlined by Krah et al. (2018) could be computed at a small step Δz right after the object entrance and right before the object exit, respectively. The resulting $y_{\mathrm{MLP}}(z = z_0 + \Delta z)$ and $y_{\mathrm{MLP}}(z = z_2 - \Delta z)$ could then be used as input for the CSP formalism. Note that y_{MLP} is not defined for $z = z_0$ and $z = z_2$ due to the argument of the logarithm in the definition of the scattering matrices σ_{t_2,θ_2}^2.

With the two methods described above, the path estimation would be optimized to include the uncertainty of the front and rear measurements in the same way as the formalism by Krah et al. (2018), but utilizing the speed of the

simple CSP formalism developed by Collins-Fekete et al. (2015). However, the full strength of the CSP algorithm lies in the fact that it does not require the parametrization of the $1/\beta^2 p^2$ function, as is necessary for the MLP approach. For the MLP-CSP hybrid outlined above, the scattering matrices need to be computed and, therefore, the parametrization of the momentum-velocity function has to be known.

In this work, we introduce a phenomenological model that enables the estimation of the optimized entrance position in the case of single sided proton radiography and CT as a function of the rear measurements and the ratio WET/WEPL to retrieve a generalized CSP formalism.

2.2. Definition of the Linear Projection Model

The LPM is a simplification of equation (23), where the scattering matrices $\left(\Sigma_2^{-1}\right)_{1,1}$ and $\left(\Sigma_2^{-1}\right)_{1,2/2,1}$ are substituted by the free parameters A_X and A_P, to be optimized through parameter scans from protons beams traversing through objects of different thicknesses and materials. Through this substitution, we can write equation (24) as

$$a = \frac{A_X}{\sigma_{t_{\text{in}}}^{-2} + A_X}, \qquad b = \frac{-A_P}{\sigma_{t_{\text{in}}}^{-2} + A_X}. \tag{26}$$

The covariance of the beam spot in the point source approximation, $\left(\Sigma_{\text{in}}^{-1}\right)_{1,1}$, has been simplified as a parallel beam to $\sigma_{t_{\text{in}}}^{-2}$. This approach preserves the model's ability to handle different incoming phase spaces in terms of beam spot sizes, and it is assumed that deviations from a parallel beam are handled by the parameter optimization. Following the notation from Collins-Fekete et al. (2015), we find the expression for the LPM

$$\mathbf{X_0}^{\text{LPM}} = \left(\frac{A_X}{\sigma_{t_{\text{in}}}^{-2} + A_X} \mathbf{X'_2} - \frac{A_P}{\sigma_{t_{\text{in}}}^{-2} + A_X} d_{\text{ph}} \mathbf{P'_2} \right) + \mathbf{X_0}^{\text{TPS}}. \tag{27}$$

In this equation, the $'$ signifies that the vector is translated around the origin defined by $\mathbf{X_0}^{\text{TPS}}$ and the beam direction $\mathbf{P_0}^{\text{TPS}}$:

$$\mathbf{X'_2} = \tilde{\mathbf{X}}_\mathbf{2} - \mathbf{X_0}^{\text{TPS}} - d_{\text{ph}} \mathbf{P_0}^{\text{TPS}} \tag{28}$$

$$\mathbf{P'_2} = \tilde{\mathbf{P}}_\mathbf{2} - \mathbf{P_0}^{\text{TPS}}. \tag{29}$$

2.3. Parameter Scans

In order to define the scalar parameters A_X and A_P, and to identify any potential energy or WET dependencies, a number of parameter scans have been performed. The Monte Carlo simulation studies were performed using GATE 8.1.p1 (Jan et al. 2011) together with Geant4 10.4.p2 (Agostinelli et al. 2003). The physics builder list `QGSP_BIC_EMZ` together with a maximum step size of 2 mm in the water phantom was chosen, and the water was modeled to have an ionization potential of 78 eV (Grevillot et al. 2010). Phantoms consisting of 0–320 mm water were irradiated by a mono-energetic 230 MeV proton pencil beam, with a Gaussian circular spot size of 3.2 mm, located at the object's entrance. The divergence and emittance of the beams were here 2 mrad and 15 mm mrad, respectively.

In each case, 10^4 protons were generated and registered at the tracker planes. For each particle, a matrix minimization parameter scan of A_P and A_X was performed. For each (A_X, A_P) pair the error was evaluated as the difference between the true and optimized beam position $|\mathbf{X_0}^{\mathrm{MC}} - \mathbf{X_0}^{\mathrm{LPM}}|$. Proton histories with high angular deviations, primarily due to (in)elastic interactions, were removed by performing a 2.5σ cut on the exit angle from $\mathbf{P'_2}$, and on the minimum residual energy of the proton exiting the phantom.§ See figure 1 for an example of a (A_X, A_P) scan, showing the average $|\mathbf{X_0}^{\mathrm{MC}} - \mathbf{X_0}^{\mathrm{LPM}}|$ error resulting from all proton histories for each parameter point.

In figure 2 the results of these scans are shown, each entry showing the optimal parameters from an optimization at a given object thickness and material. Following Collins-Fekete et al. (2015), the results are best displayed as a function of $w = \mathrm{WET}/\mathrm{WEPL}$. Exponential fits of the two parameters, applying the results from all included materials, yield the values

$$A_X = \exp\left(2.5073 - 6.3858w + 0.4913w^2\right) \tag{30}$$

$$A_P = \exp\left(1.8175 - 5.9708w - 0.8158w^2\right). \tag{31}$$

In figure 3 the a and b parameters of equation (26) from a similar LPM optimization (in water) is compared to the theoretical predictions from equation (23). Here, $\sigma_t = 3.2$ mm and 4th order polynomials are used in order to minimize the parametric difference.¶ The parameters match well, taking

§The choice of using 2.5σ as a the angular filter is motivated by Gottschalk (2012): this is the region in which the Molière scattering is well described by the Highland theory of equation (15).

¶In equations (30) and (31) a 3rd order polynomial is sufficient, since the different materials convolve the WET/WEPL dependence.

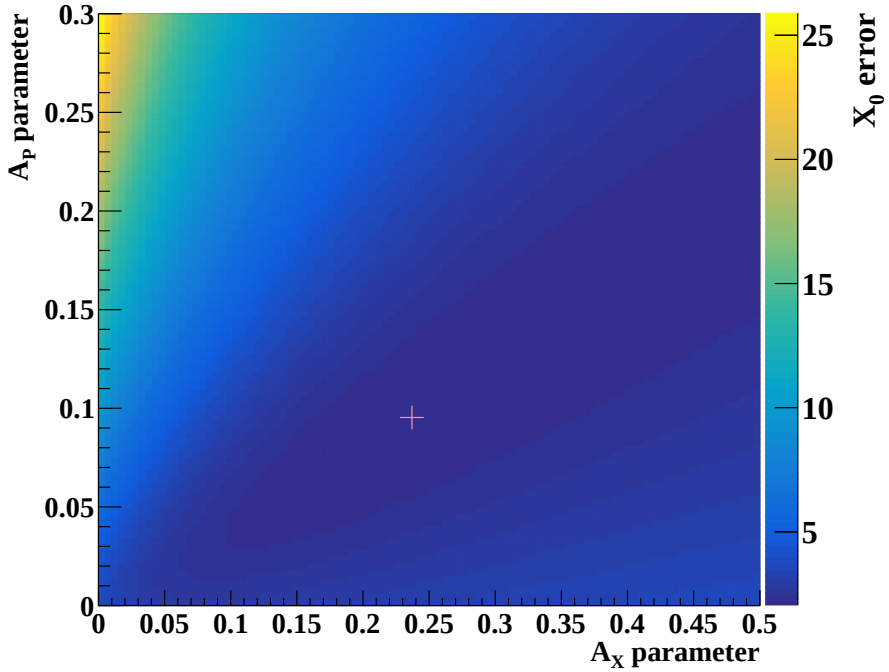

Figure 1. Parameter scan of (A_X, A_P): Each cell in the 2D histogram represents the errors between $\mathbf{X_0}^{\mathrm{MC}}$ and $\mathbf{X_0}^{\mathrm{LPM}}$: from a 200 mm water phantom irradiated by 230 MeV protons. The "+" symbol marks the cell with the lowest error.

into account that the theoretical model makes a few assumptions regarding the incoming beam phase space that are inherently accounted for in the LPM.

2.4. Phenomenological Filtering of Large Angle Scattering

The path estimation as already stated above, is based on the Fermi-Eyges approximation to multiple Coulomb scattering. Therefore, the MLP (and in extension also the CSP) formalism can only describe such particles for which the scattering in the phantom belongs to the Gaussian central part of the scattering distribution. In Schulte et al. (2008) a 3σ filter on the angular displacement of the particles was proposed to filter out the large angle scattering contribution before image reconstruction. This is usually done by finding the standard deviation directly from the particle scattering distribution, measured for each image pixel, which requires to loop through all particle histories. This adds a lot to the overall time consumption of the image reconstruction process. Additionally, the computation of the standard deviation is somewhat sensible: the large angle

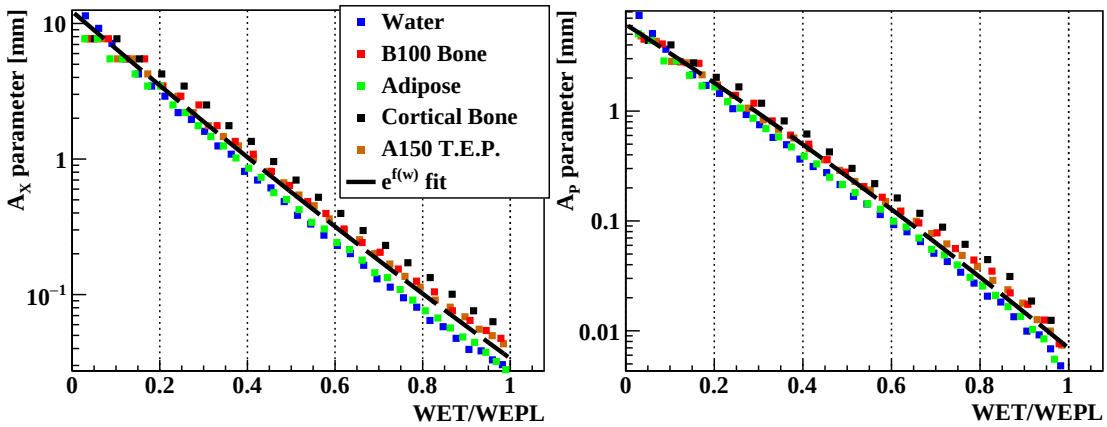

Figure 2. The A_X and A_P parameters yielding the lowest error between $\mathbf{X_0}^{\mathrm{MC}}$ and $\mathbf{X_0}^{\mathrm{LPM}}$. The exponential fit includes all materials, and their results are given in equations (30) and (31).

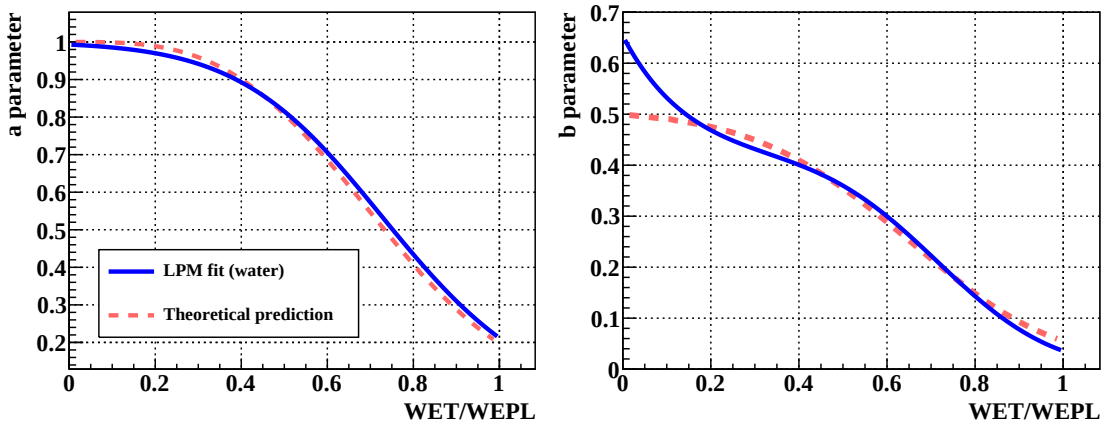

Figure 3. The factors $a = A_X \left(\sigma_{t_{\mathrm{in}}}^{-2} + A_X\right)^{-1}$ and $b = A_P \left(\sigma_{t_{\mathrm{in}}}^{-2} + A_X\right)^{-1}$ are shown as calculated from the parameter scan (equations (30) and (31)) and from the theoretical predictions (equation (24)).

scattering itself largely affects the variance of the distribution compromising the filter accuracy. The most accurate way to compute the standard deviation would be Gaussian fitting of the distribution central part, but this would be even more time consuming and is, therefore, not feasible for particle imaging. Another way would be to use the FWHM of the distribution to estimate the standard deviation.

On the other hand, it would be highly preferable to have an accurate estimate of the standard deviation without requiring an additional loop through the particle histories which could be achieved by evaluating the Fermi-Eyges scattering

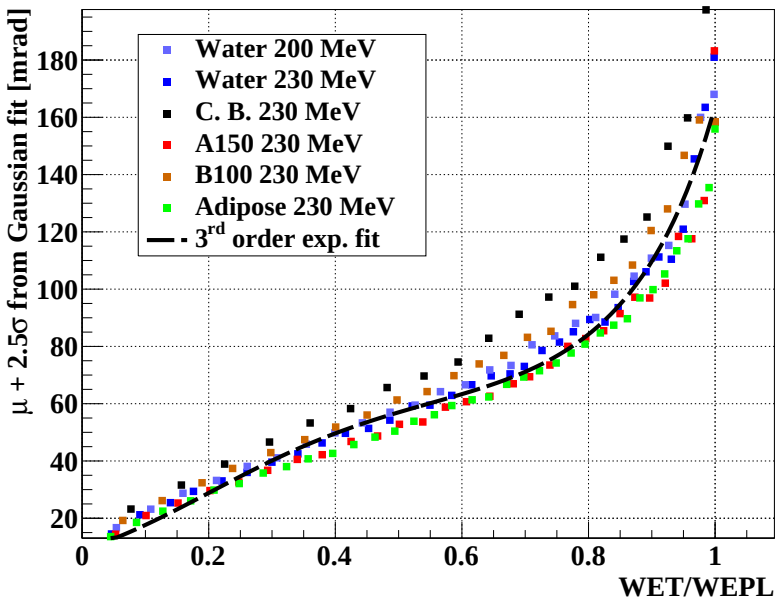

Figure 4. The phenomenological parameter fit for choosing the optimal 2.5σ value of the back tracker angles (in terms of mrad), as a function of WET/WEPL.

moments directly. However, this would require prior knowledge about the material composition of the object for the calculation of the $1/\beta^2 p^2$ function (for which again a parametrization would be needed) and the radiation length, making it very hard to implement for practical purposes. Here, we therefore propose an approximation to the standard deviation based angular displacement filtering, following the argumentation of the optimization above and the work by Collins-Fekete et al. (2015) that the scattering moments can be approximated for different materials as a function of WET/WEPL.

Figure 4 shows the 2.5σ standard deviation of the Gaussian central part of the angular displacement distribution for different materials as function of WET/WEPL as obtained by a Gaussian fit. The solid line shows an exponential fit to the data with the parameters

$$\sigma_{\theta_2,\max} = \exp\left(2.18 + 8.08w - 12.25w^2 + 7.09w^3\right), \tag{32}$$

where, again, w = WET/WEPL. Using this function, it is possible to quickly filter on the expected angular displacement of each proton individually.

3. RESULTS

The code for performing the LPM and MLP calculations and comparisons are available at `github.com/HelgeEgil/LinearProjectionModel`.

3.1. Examples of the Models

In figure 5 several proton paths are shown for protons with an initial energy of 230 MeV impinging on a water target of 160 mm thickness. The particle trajectories are estimated with the CSP formalism using the ideal measurements of $\tilde{\mathbf{X}}_\mathbf{0}$ (*i.e.*, with front tracker for comparison); with the naïve assumption that $\mathbf{X_0} = \mathbf{X_0}^{\text{TPS}}$; with the calculated $\mathbf{X_0}^{\text{LPM}}$; as well as with $\mathbf{X_0}^{\text{MLP}}$ from the extended MLP formalism for comparison. In figure 6 the RMS deviation between the estimated path and MC ground truth path are shown for using different methods to estimate the optimized entrance position (using 10^5 primary particles): the errors from $\mathbf{X_1}^{\text{MLP}}$ and $\mathbf{X_1}^{\text{LPM}}$ are visually identical and significantly lower than $\mathbf{X_1}^{\text{TPS}}$.

3.2. Phantom Dependency on Model Accuracy

The estimation error of the optimized $\mathbf{X_0}$ increases roughly linearly with the phantom size. In figure 7 the error of the LPM and extended MLP model is shown for 200 MeV and 230 MeV protons traversing through water phantoms of increasing sizes: in the case of $\mathbf{X_0}^{\text{LPM}}$, the same (A_X, A_P) parameterization was applied for both initial energies.

In figure 9, $\mathbf{X_0}^{\text{LPM}}$ is calculated in the case of five different phantom materials and varying thicknesses, and is shown as a function of the WET/WEPL ratio since their ranges are dependent on the material. The (A_X, A_P) parameters were optimized for this set of materials, and we see that the $\mathbf{X_0}^{\text{LPM}}$ accuracy is roughly similar across the materials.

3.3. Pencil Beam Spot Size Dependency on Model Accuracy

In figure 8 the the LPM and MLP models have been compared in terms of the accuracy of reproducing $\mathbf{X_0}$. The LPM has been optimized as a function of $\sigma_{t_{\text{in}}}$, and in MLP the parameters $\sigma_{t_{\text{in}}}$ and d_{source} are selected to match the beam properties — these parameters would be known in a clinical setting. We see that above $\sigma_{t_{\text{in}}} \sim 2$ mm there is little reduction of estimation accuracy due to the spot size, even up to spot sizes of 15 mm (35 mm FWHM). Below 2 mm, the $\mathbf{X_0}$ error decreases quickly towards 0.5 mm.

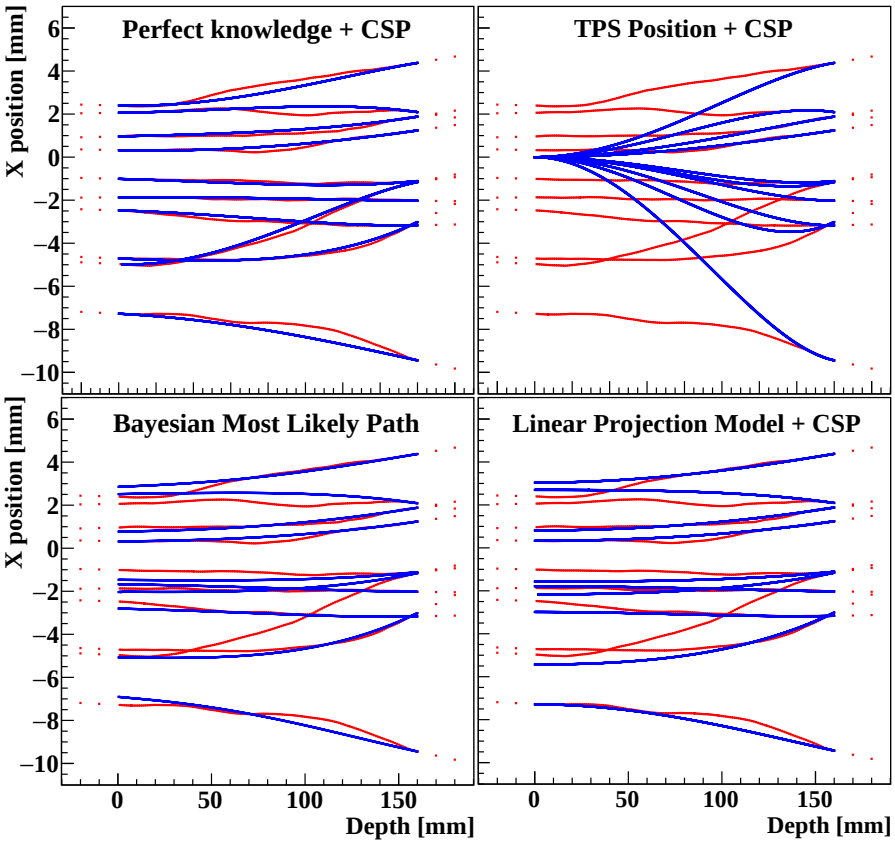

Figure 5. Examples of proton trajectory calculations with a 230 MeV proton beam in a 160 mm water phantom, using different methods to calculate the optimized $\mathbf{X_1}$ path. The red curves display the "true" $\mathbf{X_1}^{\mathrm{MC}}$ paths, while the blue curves show the various CSP or MLP $\mathbf{X_1}$ paths.

This result can be understood by looking at the role the covariance matrix of the beam spot plays in the calculation of t_0^{opt}: The larger the $\sigma_{t_{\mathrm{in}}}$, the smaller the $(\Sigma_{\mathrm{in}}^{-1})_{1,1} = (d_S \sigma_{\theta_{\mathrm{in}}})^{-2} + \sigma_{t_{\mathrm{in}}}^{-2}$ (given that the beam divergence is held fixed). Now consider

$$\left(\Sigma_{\mathrm{in}}^{-1}\right)_{1,1} \ll \left(\Sigma_2^{-1}\right)_{1,1}, \tag{33}$$

then

$$t_0^{\mathrm{opt}} = \left(\tilde{t}_2 - \theta_0^{\mathrm{TPS}} \cdot d_{\mathrm{ph}}\right) + (\tilde{\theta}_2 - \theta_0^{\mathrm{TPS}}) \frac{\left(\Sigma_2^{-1}\right)_{2,1/1,2}}{\left(\Sigma_2^{-1}\right)_{1,1}}. \tag{34}$$

In other words: For large spot sizes, the rear position is simply forward projected onto the front along the protons initial direction adding the scattering correction. Hence, the error of the position estimation plateaus with increasing spot size for

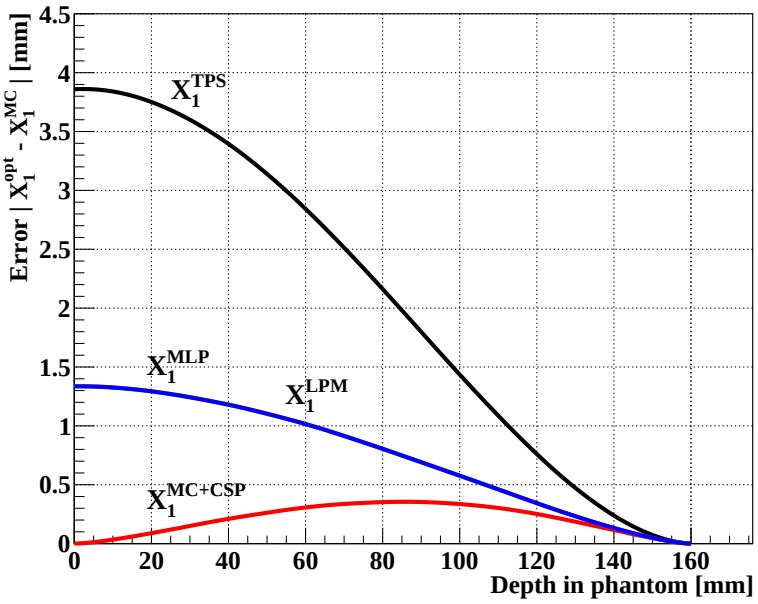

Figure 6. Errors from the Most Likely Path calculations with a 230 MeV proton beam in a 160 mm water phantom, using different methods to calculate the optimized $\mathbf{X_1}$ trajectory. The curves for $\mathbf{X_1}^{\mathrm{MLP}}$ and $\mathbf{X_1}^{\mathrm{LPM}}$ are visually identical.

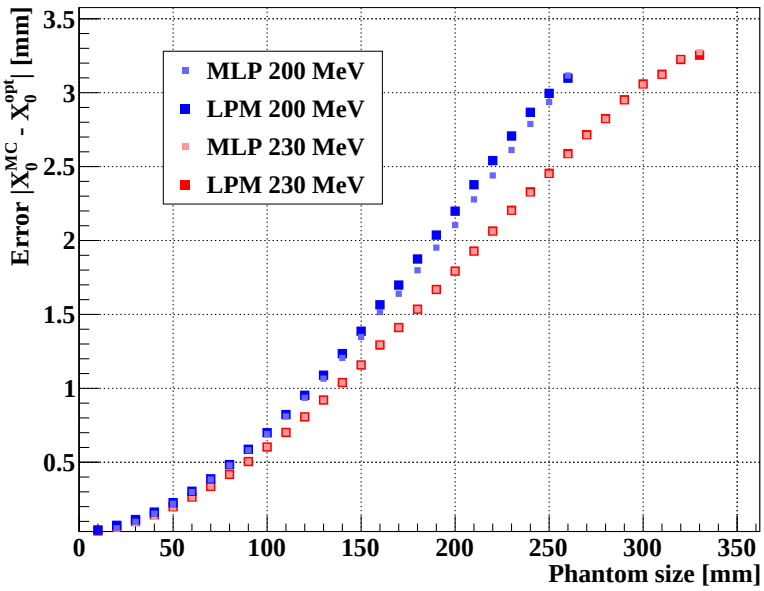

Figure 7. The error in $\mathbf{X_0}$ estimation for the two models, in terms of the initial energies 200 MeV and 230 MeV. Note that the LPM model is optimized for an initial energy of 230 MeV.

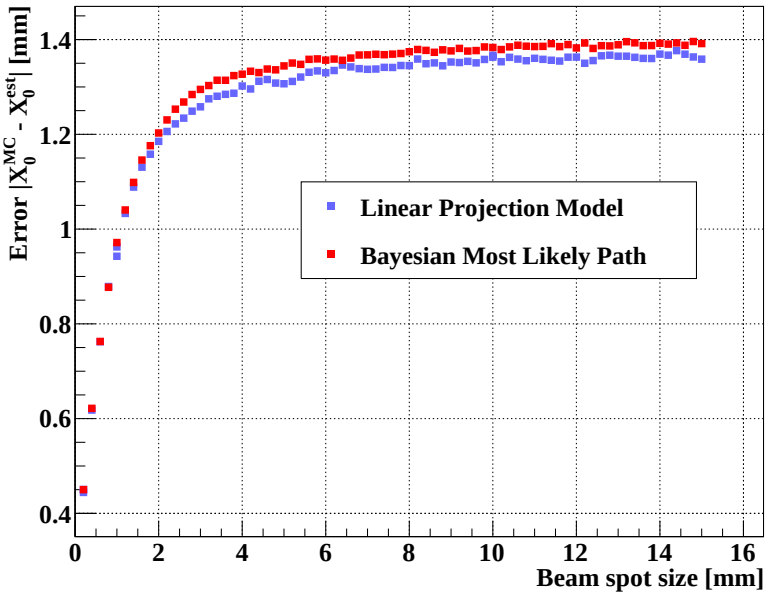

Figure 8. The $\mathbf{X_0}$ estimation errors of the two models for different beam spot sizes. The $\mathbf{X_0}^{\mathrm{LPM}}$ is calculated by using the parameters in equations (30) and (31), where $\sigma_{t_{\mathrm{in}}}$ is a model parameter.

a given phantom thickness and particle initial energy.

3.4. Comparison Between the LPM and MLP Models

In figure 7, the accuracy of the optimized entrance position resulting from the LPM was compared to that of the extended MLP formalism by Krah et al. (2018), for different energies and water phantom thicknesses (or, equivalently WET/WEPL ratios). Little to no difference between the errors of the each model prediction for $\mathbf{X_0}$ was found. However, while for the MLP, the correct parametrizations of the $1/\beta^2 p^2$ function was applied in each case, no parameters had to be changed for the LPM. Similar was observed when investigating other materials. This is also reflected in the path estimation accuracy shown in figure 6: the LPM in conjunction with the CSP results in an equally accurate path estimation compared to what would be achievable with the extended MLP algorithm.

The $\mathbf{X_0}$ estimation accuracy is kept constant when the the initial angle $\mathbf{P_0}^{\mathrm{TPS}}$ is increased. This holds for initial angles far above the typical values for clinical pencil beam angles (Grevillot et al. 2011).

In terms of computational time, it has been found the Bayesian MLP method

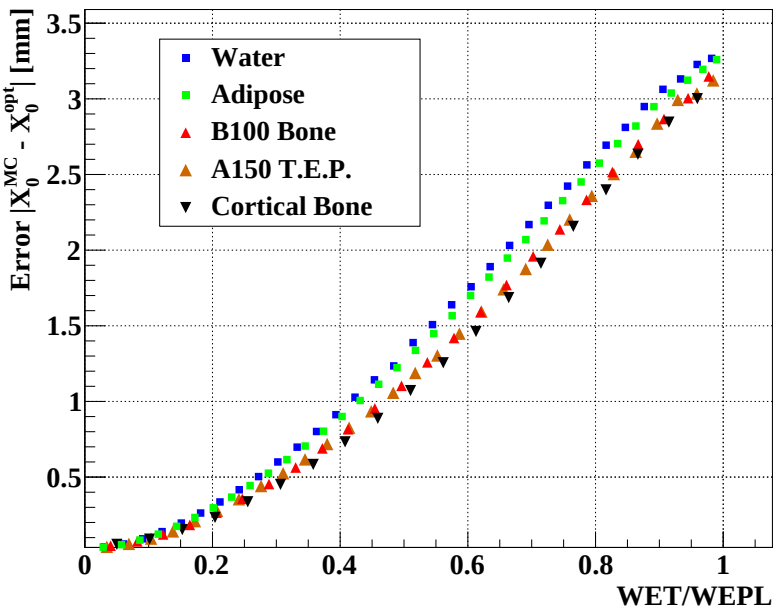

Figure 9. Errors from $\mathbf{X_0}^{\mathrm{LPM}}$ in five different ICRU materials: Water, Adipose, B100 Bone, A150 Tissue Equivalent Plastic and Cortical Bone. The initial beam is a 230 MeV proton beam.

described is approximately 15 times more demanding compared to the LPM in conjunction with the CSP algorithm. This benefit is only slightly reduced when using the CSP in conjunction with the theoretical prediction from equation (23) instead of the LPM parameters. These numbers are reflected in Collins-Fekete et al. (2015), and the difference can be crucial when considering that ∼200 million protons are used in a volumetric CT reconstruction: the CSP can be optimized to include just the same generality as the extended MLP formalism but using only a fraction of the time.

3.5. Application of LPM to Helium Imaging

Since recently rising interest has been placed in helium ion imaging (Collins-Fekete et al. 2017a, Volz et al. 2017, Piersimoni et al. 2018, Gehrke et al. 2018, Volz et al. 2018, Martišíková et al. 2018), we show that the methods developed in this work are applicable to single-sided helium imaging as well. The theoretical prediction of equation (23) is directly applicable to other ion species, if the scattering moments are scaled by a factor of the ion charge squared (z^2) and the appropriate parametrization of the $1/\beta^2 p^2$ function is used.

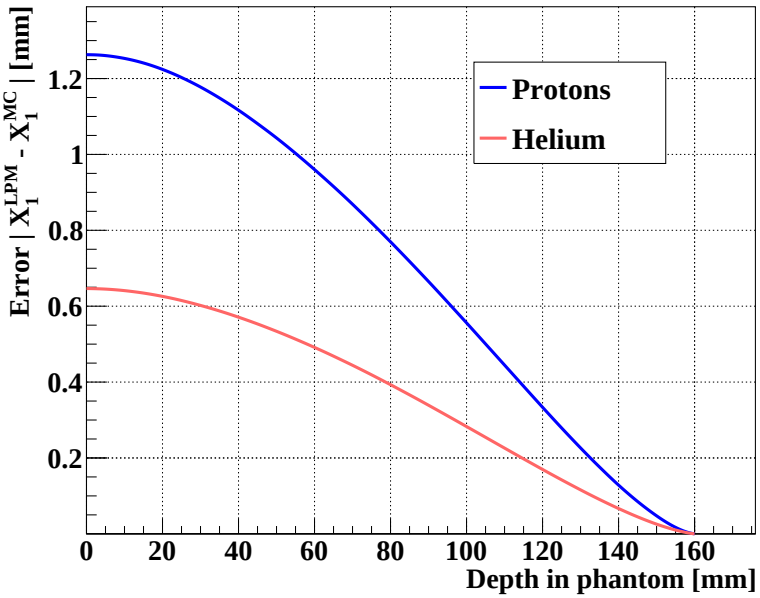

Figure 10. The error in $\mathbf{X_1}$ estimation between protons and Helium ions, having equal WEPL ranges (33 cm) and beam spot sizes (3 mm).

Since for helium the $1/\beta^2 p^2$ function scales with a factor of one over the atomic mass squared ($1/A^2$) to that of protons (Collins-Fekete et al. 2017a, Gehrke et al. 2018), the inverse scattering matrix elements in equation (24) only have to be scaled by a factor $A^2/z^2 = 4$ compared to that of protons:

$$(\Sigma_2^{-1})^{\alpha}_{1,1} = 4 \times (\Sigma_2^{-1})^{\mathrm{p}}_{1,1}, \qquad (\Sigma_2^{-1})^{\alpha}_{1,2/2,1} = 4 \times (\Sigma_2^{-1})^{\mathrm{p}}_{1,2/2,1} \tag{35}$$

A beam of 230 MeV/u Helium with $\sigma_{t_{\mathrm{in}}} = 3$ mm was simulated through a 160 mm water phantom, and an set of optimized model parameters was found. The resulting $|\mathbf{X_0}^{\mathrm{LPM}} - \mathbf{X_0}^{\mathrm{MC}}|$ accuracy is 0.65 mm, half the value of 1.26 mm for 230 MeV protons. This is expected from the scattering matrices, since the displacement resulting from multiple coulomb scattering is a factor 2 smaller for helium ions compared to protons (Collins-Fekete et al. 2017a, Gehrke et al. 2018). The deviation between the optimized CSP based on the LPM entrance position and the MC ground truth path for protons and helium ions in this scenario is shown in figure 10.

3.6. Measurement Uncertainties and Model Accuracy

In the extended MLP model (Krah et al. 2018), a term describing the uncertainties in the $\tilde{\mathbf{X}}_\mathbf{2}$ and $\tilde{\mathbf{P}}_\mathbf{2}$ measurements can be added to equation (8), such that

$$C_2 = R_1^{-1} S_{\text{out}}^{-1} \Sigma_{\text{out}} \left(S_{\text{out}}^{-1}\right)^{\mathsf{T}} \left(R_1^{-1}\right)^{\mathsf{T}} + R_1^{-1} \Sigma_2 \left(R_1^{-1}\right)^{\mathsf{T}}, \tag{36}$$

where

$$\Sigma_{\text{out}} = \sigma_p^2 \begin{pmatrix} 0 & 1 \\ -1/d_T & 1/d_T \end{pmatrix} \cdot \begin{pmatrix} 0 & -1/d_T \\ 1 & 1/d_T \end{pmatrix} + \begin{pmatrix} 0 & 0 \\ 0 & \sigma_{\text{sc}}^2 \end{pmatrix}. \tag{37}$$

The uncertainties of the hit position on the tracker, and on the hit direction due to scattering in the first tracker layer, are given as σ_p and σ_{sc}, respectively. The distance between the two back trackers needed to calculate $\tilde{\mathbf{P}}_\mathbf{2}$ is d_T.

To introduce uncertainties in terms of position σ_p and scattering σ_{sc} in the $\tilde{\mathbf{X}}_\mathbf{2}$ and $\tilde{\mathbf{P}}_\mathbf{2}$, as found from the ideal detectors in MC, the following procedure has been chosen (described in one dimension): First, find the ideal angle θ_2 from $\tilde{\mathbf{P}}_\mathbf{2}$. Then, sample the Gaussian distribution $G(\mu, \sigma)$ to find the perturbed (scattered) angle θ_2^σ. To mimic realistic measurements, x_2^σ and x_3^σ on the back tracker, we get

$$\theta_2^\sigma = G\left(\theta_2, \sigma_{\text{sc}}\right) \tag{38}$$

$$x_2^\sigma = G(x_2, \sigma_p) \tag{39}$$

$$x_3^\sigma = G(x_2^\sigma + d_T \theta_2^\sigma, \sigma_p). \tag{40}$$

Then, $\mathbf{X}_\mathbf{2}^\sigma$ and $\mathbf{P}_\mathbf{2}^\sigma$ are calculated from equations (39) and (40), and they are used to calculate $\mathbf{X}_\mathbf{0}^{\text{MLP}}$ taking into account σ_p and σ_{sc} as described above, and $\mathbf{X}_\mathbf{0}^{\text{LPM}}$. Note that the final direction vector $\mathbf{P}_\mathbf{2}^\sigma$ takes into account both the added scattering and the added position uncertainty of both of the tracker planes.

The loss in accuracy after introducing tracker uncertainties are here calculated in two contexts: The proton CT scanner of Bashkirov et al. (2016) (with front trackers removed) where $\sigma_p \simeq 66\,\mu\text{m}$ and $\sigma_{\text{sc}} \simeq 10\,\text{mrad}$, and a single sided proton CT scanner under development (Pettersen et al. 2017) with expected properties of $\sigma_p \sim 8\,\mu\text{m}$ and $\sigma_{\text{sc}} \sim 7\,\text{mrad}$.

In figure 11 the $\mathbf{X}_\mathbf{0}^{\text{LPM}}$ and $\mathbf{X}_\mathbf{0}^{\text{MLP}}$ accuracy from the two setups are shown, compared to using ideal back trackers. In general the two models perform similarly, however $\mathbf{X}_\mathbf{0}^{\text{MLP}}$ outperforms $\mathbf{X}_\mathbf{0}^{\text{LPM}}$ for the small-to-medium phantoms, and vice versa for the larger phantoms.

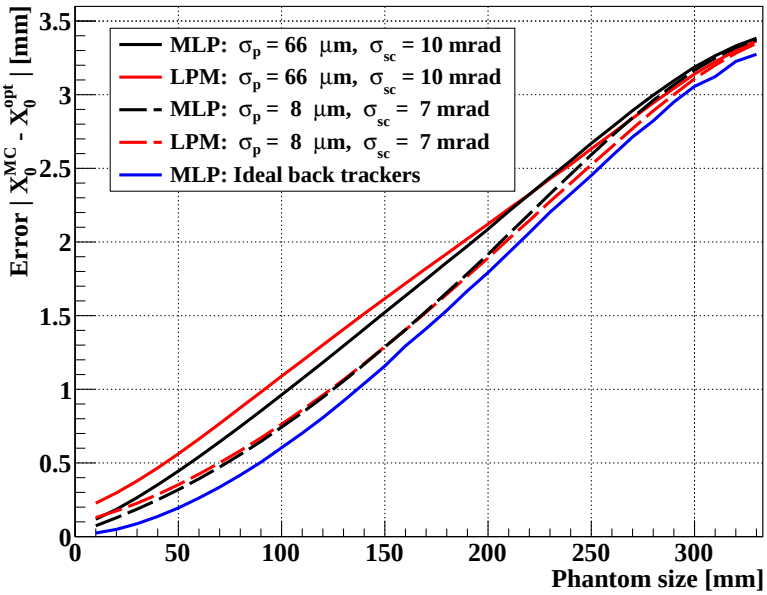

Figure 11. The expected $\mathbf{X_0}^{\mathrm{opt}}$ accuracy degradation by uncertainties in the $\tilde{\mathbf{X}}_\mathbf{2}$ measurements due to scattering between the tracker layers and the RMS resolution of the position measurements (Johnson 2018).

4. DISCUSSION

In this work, we have presented a simplified version of the extended MLP by Krah et al. (2018) that can be used for single sided proton imaging. In the method, first an optimized guess of the particle entrance point is found — either by taking into account the beam's phase-space and updating that information using the rear tracker measurement combined with Fermi-Eyges' approximation to Molière's scattering theory; or by a phenomenological optimization based on two parameters as a function of WET/WEPL. This optimized entrance point is then used as input for the optimized CSP algorithm by Collins-Fekete et al. (2015). It is noted, that a similar approach to a MLP-CSP hybrid formalism has been investigated in Brooke & Penfold (2018) to include the material dependence of the MLP into the CSP formalism. In their formalism, the MLP would be computed at several steps through the object to account for material heterogeneity and a CSP would be interpolated in between the so derived points. However, in that work, no considerations on tracker uncertainties or single sided proton imaging is made.

In the derivation of the method developed here, two assumptions have been made: first we assumed that the beam delivery system is relatively trustworthy

regarding the beam direction, such that each proton entered the object with the direction specified by the TPS. This assumption can be justified by the fact that the scattering deflection in the object is much greater than the deviation of the particle's initial direction stemming from uncertainties in the beam delivery system. A difference between the optimized and the theoretical parameters is observed. This is likely related to the fact that for small object thicknesses, the multiple scattering of the particles is less pronounced and, therefore, the initial direction uncertainty can not be neglected in the parameter optimization. The phenomenological optimization naturally takes this into account, resulting in the observed deviation between theoretically predicted and optimized parameters at small WET/WEPL ratios. For simulations using an ideal parallel beam, the theoretical and optimized parameters overlap even for small WET/WEPL ratios. However, the models perform equally well in terms of predicting the initial position of each proton.

The second assumption was that of an ideal rear tracker. While in general, the uncertainty of the rear tracker could be included by building the model based on equation (16), the results shown in this work indicate that the potential benefit would be minor as introducing artificially the uncertainty of different detector systems to the measurement of the outgoing particles direction did not have a large impact on the model accuracy when compared to the gold standard represented by the extended MLP algorithm. Especially for the system envisioned by Pettersen et al. (2017), the difference between the two approaches is negligible.

Also, a drawback of the method is that it requires the proton measurements to be distinctly connectable to the spot scanning information. This requires either the detector capable of assigning a time stamp to each proton hit that can then be connected to the TPS information, or, in the case of the system envisioned by Pettersen et al. (2018), the acquisition frame rate of the detector to be faster than the time interval between individual spots to avoid several spots to be contained in one read out frame.

The main advantage of the method proposed here is that it allows to utilize the favorable computational speed of the CSP algorithm without compromising the path estimation accuracy compared to the extended MLP algorithm. Both the theoretical derivation of the optimal entrance point and the phenomenological optimization yielded similar results in this work. However, the phenomenological optimization offers the additional benefit, that it does not require the implementation of the scattering matrices and, therefore, the correct description of the $1/\beta^2 p^2$ function. It is simple to implement and is valid in

the same way for different energies and materials without a large increase in the uncertainty.

Moreover, the model could also directly be applied for implementing a front tracker to the detector system envisioned by Pettersen et al. (2018) even despite the large multiplicity measured simultaneously: the model definition space would become a discrete set of measurements taken at the front tracker. For each proton, the most likely corresponding front tracker measurement could then be found simply as the proton hit closest to $\mathbf{X_0}^{\mathrm{LPM}}$, given, that the detector system's acquisition frame rate is faster then the spot scanning.

Additionally, it was shown that the model is directly applicable for other ion species as well, and a comparison of protons and helium ions was drawn. Here, it was seen that the smaller lateral displacement of helium ions compared to that of protons results in a factor 2 improvement of the estimation of the particle entrance position for a fixed beam focus, consequently increasing the path estimation accuracy. Additionally, when looking at current beam delivery systems, the lower scattering of helium ions in the beam monitoring system and the air between nozzle and patient would enable a smaller achievable focus at the isocenter. This indicates that the favorable spatial resolution achievable with helium ions over protons in particle list-mode imaging outlined by Collins-Fekete et al. (2017a) and Gehrke et al. (2018) would translate even more so to single-sided setups.

The argumentation for the LPM presented in this work is not limited to single sided proton imaging: the full generality of the extended MLP estimation lies within the two likelihoods presented in equation (16), and equation (17). Maximizing these likelihoods yields the optimized entrance and exit parameter vectors that can be used as an input to the optimized CSP algorithm by Collins-Fekete et al. (2015) for any particle list mode imaging device. This could even be used in conjunction with the MLP algorithm by Schulte et al. (2008) and still be slightly less time consuming than the extended MLP algorithm, as it would require the consideration of the tracking uncertainties only once instead of at every step through the object. Hence, existing MLP implementations would not have to be changed and only the optimization of the input vectors would have to be added to the reconstruction code. This advantage in implementation complexity and computational speed comes at no loss of accuracy: the method outlined in this paper yields exactly the same results as would be obtained with the extended MLP formalism by Krah et al. (2018) in cases where only the proton trajectory is relevant. Only if the uncertainty envelope around the MLP is of interest, the

extended MLP algorithm is the more adapt formalism.

As a side result of this work, it was shown that the accuracy of the estimation of the entrance point of the particles is not sensitive to the beam spot sigma for broader pencil beams. However, a beam spot sigma smaller than 2 mm — as was already proposed by Hanson et al. (1978) — would greatly benefit the path estimation. This is in line with the conclusion on the spatial resolution by Krah et al. (2018), since a better estimate of the entrance position benefits the path estimation and, hence, the spatial resolution achievable. Future work on single sided proton imaging therefore should go hand in hand with the development of accurate beam delivery systems — with the thin pencil beam focusing recently demonstrated by Farr et al. (2018), accurate single sided proton imaging does not seem a far fetched goal.

Additionally, in this work, as simple approach to filter out large angle scattering events based on a WET/WEPL parametrization of the particle angular displacement has been proposed. The method relies on the observation, that the scattering moments can be approximated for different materials and phantom thicknesses as a function of WET/WEPL. The downside of this method is that it depends on the accuracy of the WET measurement of the detector. However, for current prototypes, as for example the detector system outlined by Bashkirov et al. (2016), the WET accuracy is comparable to the range straggling of the particles which for protons is $\sim$1% of the initial range. Comparing with figure 4, the difference in the 2.5σ parametrization for a WET uncertainty of 3.3 mm (in the case of 230 MeV protons) is negligible. The main advantage of the proposed method is that it does not need the computation of the scattering distribution which requires looping over all particle histories before image reconstruction, but can be performed on a particle-by-particle approach, vastly improving the reconstruction speed.

5. CONCLUSIONS

In this study, we have shown the feasibility of estimating the individual beam spot positions from measurements of the proton's position and direction downstream to the patient. This is a required approach in single sided proton CT, where the incoming position is not measured and must be estimated in order to find its trajectory through the patient.

Two different approaches to the calculation of an optimized incoming position have been considered: a likelihood model based on Fermi-Eyges approximation

to Molière's scattering theory together with the position and direction of the proton beam set in the treatment planning system; and a simpler linear projection model where the scattering theory contribution is replaced by two optimized model parameters. The two methods yield similar results, in terms of accuracy and computational demand, however the linear projection model outperforms the likelihood model in terms of implementation complexity. The model prediction for the incoming proton position was used as input for the optimized cubic spline path algorithm. The results were compared to the gold standard represented by the recently extended MLP algorithm and the approach presented in this work yields a great advantage in terms of computational demand while coming at no loss of accuracy. We therefore conclude, that the approach presented in this work is a efficient and easy to implement version of the extended MLP formalism and has a great potential for single sided proton list mode imaging.

References

Agostinelli, S., Allison, J., Amako, K., Apostolakis, J., Araujo, H., Arce, P., Asai, M., Axen, D., Banerjee, S., Barrand, G. et al. (2003). Geant4—a simulation toolkit, *Nuclear Instruments and Methods in Physics Research Section A: Accelerators, Spectrometers, Detectors and Associated Equipment* **506**(3): 250–303.

Bashkirov, V. A., Schulte, R. W., Hurley, R. F., Johnson, R. P., Sadrozinski, H. F.-W., Zatserklyaniy, A., Plautz, T. & Giacometti, V. (2016). Novel scintillation detector design and performance for proton radiography and computed tomography, *Medical Physics* **43**(2): 664–674.

Berger, M. J., Coursey, J., Zucker, M. & Chang, J. (2005). *ESTAR, PSTAR, and ASTAR: Computer Programs for Calculating Stopping-Power and Range Tables for Electrons, Protons, and Helium Ions*, National Institute of Standards and Technology.
URL: *http://physics.nist.gov/Star*

Brooke, M. & Penfold, S. (2018). An inhomogeneous most likely path formalism for proton computed tomography, *ArXiv e-prints* .

Collins-Fekete, C.-A., Brousmiche, S., Hansen, D. C., Beaulieu, L. & Seco, J. (2017a). Pre-treatment patient-specific stopping power by combining list-mode proton radiography and x-ray CT, *Physics in Medicine and Biology* **62**(17): 6836.

Collins-Fekete, C.-A., Doolan, P., Dias, M. F., Beaulieu, L. & Seco, J. (2015). Developing a phenomenological model of the proton trajectory within a heterogeneous medium required for proton imaging, *Physics in Medicine and Biology* **60**(13): 5071–5082.

Collins-Fekete, C.-A., Volz, L., Portillo, S. K. N., Beaulieu, L. & Seco, J. (2017b). A theoretical framework to predict the most likely ion path in particle imaging, *Physics in Medicine and Biology* **62**(5): 1777–1790.

Farr, J. B., Moskvin, V., Lukose, R. C., Tuomanen, S., Tsiamas, P. & Yao, W. (2018). Development, commissioning, and evaluation of a new intensity modulated minibeam proton therapy system, *Medical Physics* **45**(9): 4227–4237.

Gehrke, T., Amato, C., Berke, S. & Martišíková, M. (2018). Theoretical and experimental comparison of proton and helium-beam radiography using silicon pixel detectors, *Physics in Medicine and Biology* **63**(3): 035037.

Gottschalk, B. (2012). Techniques of proton radiotherapy: transport theory, *arXiv:1204.4470* . **URL:** *http://arxiv.org/abs/1204.4470*

Grevillot, L., Bertrand, D., Dessy, F., Freud, N. & Sarrut, D. (2011). A Monte Carlo pencil beam scanning model for proton treatment plan simulation using GATE/GEANT4, *Physics in Medicine and Biology* **56**(16): 5203.

Grevillot, L., Frisson, T., Zahra, N., Bertrand, D., Stichelbaut, F., Freud, N. & Sarrut, D. (2010). Optimization of GEANT4 settings for Proton Pencil Beam Scanning simulations using GATE, *Nuclear Instruments and Methods in Physics Research Section B: Beam Interactions with Materials and Atoms* **268**(20): 3295–3305.

Hanson, K. M., Bradbury, J. N., Cannon, T. M., Hutson, R. L., Laubacher, D. B., Macek, R., Paciotti, M. A. & Taylor, C. A. (1978). The application of protons to computed tomography, *IEEE Transactions on Nuclear Science* **25**(1): 657–660.

Jan, S., Benoit, D., Becheva, E., Carlier, T., Cassol, F., Descourt, P., Frisson, T., Grevillot, L., Guigues, L., Maigne, L. et al. (2011). GATE V6: a major enhancement of the GATE simulation platform enabling modelling of CT and radiotherapy, *Physics in Medicine and Biology* **56**(4): 881–901.

Johnson, R. P. (2018). Review of medical radiography and tomography with proton beams, *Reports on Progress in Physics* **81**(1): 016701.

Krah, N., Khellaf, F., Rit, S. & Rinaldi, I. (2018). A comprehensive theoretical comparison of proton imaging set-ups in terms of spatial resolution, *Physics in Medicine and Biology* **63**(13).

Li, T., Liang, Z., Singanallur, J. V., Satogata, T. J., Williams, D. C. & Schulte, R. W. (2006). Reconstruction for proton computed tomography by tracing proton trajectories: A Monte Carlo study, *Medical Physics* **33**(3): 699.

Martišíková, M., Gehrke, T., Berke, S., Aricò, G. & Jäkel, O. (2018). Helium ion beam imaging for image guided ion radiotherapy, *Radiation Oncology* **13**(1).

Pettersen, H. E. S., Alme, J., Biegun, A., van den Brink, A., Chaar, M., Fehlker, D., Meric, I., Odland, O. H., Peitzmann, T., Rocco, E. et al. (2017). Proton tracking in a high-granularity Digital Tracking Calorimeter for proton CT purposes, *Nuclear Instruments and Methods in Physics Research Section A: Accelerators, Spectrometers, Detectors and Associated Equipment* **860C**: 51–61.

Pettersen, H. E. S., Chaar, M., Meric, I., Odland, O. H., Sølie, J. R. & Röhrich, D. (2018). Accuracy of parameterized proton range models; a comparison, *Radiation Physics and Chemistry* **144**: 295–297.

Piersimoni, P., Faddegon, B. A., Méndez, J. R., Schulte, R. W., Volz, L. & Seco, J. (2018). Helium CT: Monte Carlo simulation results for an ideal source and detector with comparison to proton CT, *Medical Physics* **45**(7): 3624–3274.

Schulte, R. W., Penfold, S. N., Tafas, J. T. & Schubert, K. E. (2008). A maximum likelihood proton path formalism for application in proton computed tomography, *Medical Physics* **35**(11): 4849.

Volz, L., Collins-Fekete, C.-A., Piersimoni, P., Johnson, R. P., Bashkirov, V., Schulte, R. & Seco, J. (2017). Stopping power accuracy and achievable spatial resolution of helium ion

imaging using a prototype particle ct detector system, *Current Directions in Biomedical Engineering* **3**: 401.

Volz, L., Piersimoni, P., Bashkirov, V. A., Brons, S., Collins-Fekete, C.-A., Johnson, R. P., Schulte, R. W. & Seco, J. (2018). The impact of secondary fragments on the image quality of helium ion imaging, *Physics in Medicine and Biology* **63**(19): 195016.

Williams, D. C. (2004). The most likely path of an energetic charged particle through a uniform medium, *Physics in Medicine and Biology* **49**(13): 2899–2911.

Zygmanski, P., Gall, P. K., Rabin, M. S. & Rosenthal, S. J. (2000). The measurement of proton stopping power using proton-cone-beam computed tomography, *Physics in Medicine and Biology* **45**(2): 511–28.